Moiré impurities in twisted bilayer black phosphorus: Effects on the carrier mobility

Peng Kang,[1,2,*] Wan-Ting Zhang,[2,3] Vincent Michaud-Rioux,[2] Xiang-Hua Kong,[2] Chen Hu,[2] Guang-Hua Yu,[1] and Hong Guo[2]

[1]*School of Materials Science and Engineering, University of Science and Technology Beijing, Beijing, 100083, People's Republic of China*

[2]*Center for the Physics of Materials and Department of Physics, McGill University, Montreal, Quebec, Canada, H3A 2T8*

[3]*School of Mechanical, Electronic, and Information Engineering, China University of Mining and Technology (Beijing), Beijing, 100083, People's Republic of China*

(Received 11 September 2017; revised manuscript received 24 October 2017; published 6 November 2017)

Moiré patterns on two-dimensional van der Waals heterostructure can give rise to unique electronic and transport properties. In this work we report a theoretical investigation of Moiré patterns on twisted bilayer black phosphorus (tbBP). It is found that the Moiré pattern has extraordinary effects and leads to significant asymmetry with respect to transport direction and carrier type. The high-symmetry local stacking configurations in the Moiré pattern act as impurities with sizes at the Moiré length scale, and these "Moiré impurities" induce flatbands and localized states in tbBPs. Because both the conduction band minimum and valence band maximum are dominated by these localized states, the deformation potential limited carrier mobility is significantly affected: the electron mobility of tbBPs reduces by almost 20-fold when twisting from zero angle ($\sim$2560 $\mathrm{cm^2\,V^{-1}\,s^{-1}}$) to just 1.8° ($\sim$131 $\mathrm{cm^2\,V^{-1}\,s^{-1}}$). The microscopic physics behind these effects are revealed by the real-space wave functions.

DOI: 10.1103/PhysRevB.96.195406

I. INTRODUCTION

Two-dimensional (2D) materials have attracted great attention due to their unique properties with respect to those of their parent compounds [1–4]. More recently, 2D materials were found to form van der Waals (vdW) heterostructures, which significantly expanded the material phase space of the 2D world [5–10]. In a vdW heterostructure made by stacking two layers on top of each other, such as graphene on hexagonal boron nitride (*h*BN) [11–13], bilayer transition-metal dichalcogenides (TMDC) [14–16], twisted bilayer graphene [17–21], etc. Moiré patterns are often observed experimentally due to a small lattice mismatch or relative rotation of the two constituent layers. A Moiré pattern is an optical perception of a new pattern when two patterns are stacked together. In 2D vdW materials, however, a Moiré pattern is a physical superlattice which brings about surprising electronic properties, including the Hofstadter butterfly [22] and topological states [23].

Of the many 2D materials, the monolayer black phosphorus (BP) stands out as an emerging electronic material [24] due to its tunable direct band gap [25], predicted high carrier mobility [26], anisotropic Landau levels [27,28], and interesting anomalous magneto-optical transport properties [29–31]. The material quality of BP is further enhanced by *h*BN encapsulation, forming a vdW heterostructure [32]. The twist angle between the two monolayer BPs [33] results in diverse stacking orders [34,35] whereby a variety of different *high-symmetry local stacking configurations* are simultaneously present in a twisted bilayer BP (tbBP) – appearing as the Moiré pattern. As an example, Fig. 1(a) shows the formation and the Moiré pattern on a tbBP when the two monolayer BP lattices are rotated by a small angle relative to each other. In this case, there are four high-symmetry local stacking configurations, named AA, AB, AA' and AB', indicated by the colored rectangles in Fig. 1(b). Because the interactions between the atoms in the two monolayer BPs are different in these different local configurations, the electronic potential of the tbBP is in fact not a "flatland" but a "rugged land" (Appendix B). Clearly, such rugged-land potential is expected to lead to extraordinary effects to carrier transport when the twisted bilayer is applied in electronic devices.

It is the purpose of this work to theoretically investigate how the carrier mobility of bilayer BP is affected by the Moiré patterns when the two monolayer BP lattices are rotated by a small twist angle θ. Intuitively, one may consider the high-symmetry local stacking configurations in the Moiré pattern as big "impurities" periodically residing in an infinitely large 2D bilayer. For instance, the red rectangle in Fig. 1(b), namely, the AA stacking configuration, is periodically extended to form the Moiré superlattice, so are the other colored rectangles. By direct first-principles calculations, we discover that these "Moiré impurities" form flat impurity bands at both the conduction band minimum (CBM) and valence band maximum (VBM) of the tbBP, and these flatbands are caused by the localization of the electronic wave functions along certain directions. As a result, the phonon limited carrier mobility is drastically affected: at a rotation of $\theta = 1.8°$, the electron mobility ($\sim$131 $\mathrm{cm^2\,V^{-1}\,s^{-1}}$) is almost 20 times smaller than that of the perfectly matching bilayer ($\sim$2560 $\mathrm{cm^2\,V^{-1}\,s^{-1}}$). Such an extraordinary effect is completely attributable to the formation of periodic "Moiré impurities."

The paper is organized as follows: Section II presents a structural model and theoretical methods. Our results are discussed in Sec. III, and Sec. IV is reserved for a short summary. Finally, relevant methodological details and additional results are included in several Appendices.

II. MODEL AND METHOD

The tbBP is constructed by rotating one constituent BP lattice a certain small angle θ with respect to the other BP lattice, as shown in Fig. 1(a). Roughly speaking, the length scale of the Moiré pattern is proportional to $1/\theta$ [17,36]. Without loss of generality, we shall investigate tbBP with small

*kangp@physics.mcgill.ca

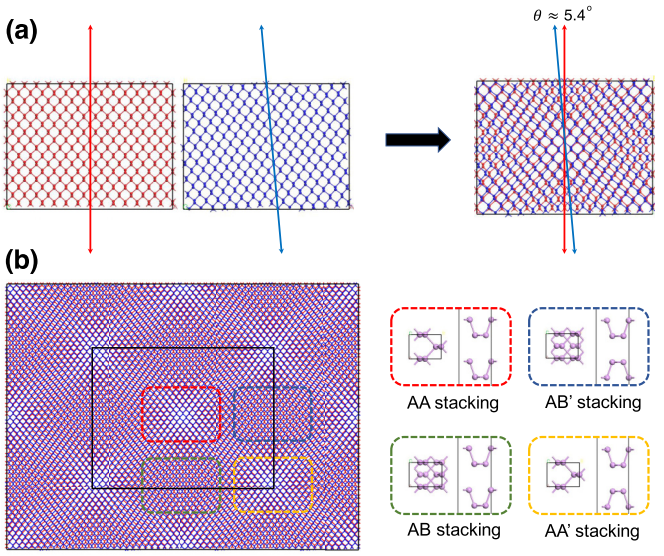

FIG. 1. (a) Schematic construction of a tbBP with a small twisted angle θ which is defined by the orientation between the two constituent BP lattices. The zero angle corresponds to the AA stacking of bilayer BP. (b) Moiré pattern formed on the tbBP with $\theta = 2.7^\circ$. The colored rectangles indicate the distribution of the high-symmetry local stacking configurations in tbBPs and the black rectangle indicates the simulated 2.7-tbBP supercell containing 3588 atoms. The atomic structures of the four high-symmetry local stacking configurations, named AA, AB, AA', and AB', are shown in the right panel.

twist angles $\theta = 1.8^\circ, 2.2^\circ, 2.7^\circ, 3.6^\circ, 5.4^\circ$, in which the Moiré patterns are relatively large. The structural details of the tbBP are listed in Table I. The untwisted BP [uBP, left red BP in Fig. 1(a)], which is one of the two constituent monolayer BPs, is formed by replicating the primitive cell of BP (e.g., AA stacking) by a factor of p and n along the x and y directions, respectively. The twisted BP [tBP, right blue BP in Fig. 1(a)] is formed by rotating the uBP by an angle θ. The black rectangle in the left panel of Fig. 1(b) delimits the simulated tbBP supercell for $\theta = 2.7^\circ$ (named "2.7-tbBP" thereafter); it contains 3588 atoms and the supercell dimensions are 93.90 Å × 70.98 Å. Note that it is necessary to calculate these very large tbBP supercells in order to essentially remove any significant lattice mismatch between the tBP and uBP (see Table I), which is important to predict the intrinsic properties of tbBP. The largest structure in our investigation ($\theta = 1.8^\circ$) contains 8068 atoms.

For these large tbBP supercells, the structural relaxation and analysis of mechanical properties are carried out by force fields as implemented in the large-scale atom/molecular massively parallel simulator (LAMMPS) [37]. The in-plane interactions between the atoms are treated at the many-body Stillinger-Weber (SW) potential level [38], which has been validated by first-principles method. The interlayer vdW interaction is described by a Lennard-Jones (LJ) potential [39]. The relaxation is completed when the residual force per atom is less than 1.0×10^{-6} eV/Å.

Having determined the atomic structures of the tbBP with twist angles θ, the electronic and transport properties (carrier mobility) are calculated by Kohn-Sham density functional theory (KS-DFT). Performing KS-DFT self-consistent analysis on such large 2D systems is a numerical challenge [40] which has been met by our recently developed real-space KS-DFT method RESCU [41]. Very briefly, RESCU uses the Chebyshev filtering technique [42] to avoid fully diagonalizing the large Kohn-Sham eigenvalue problem, and it applies advanced computational mathematics to achieve a high parallelization efficiency. For technical details we refer interested readers to the original literature [41]. In the KS-DFT self-consistent calculation, a single Γ-point reciprocal space sampling is adequate for the tbBP structures, since the Brillouin zone (BZ) is extremely small as a result of the large supercell size. A Γ-centered 12 × 14 × 1 Monkhorst-Pack grid is used in the self-consistent KS-DFT calculations for the individual high-symmetry local stacking configurations. The atomic cores are pseudoized using the optimized norm-conserving Vanderbilt (ONCV) scheme [43]. The exchange-correlation energy is treated using the generalized gradient approximation (GGA) [44] for band structure calculations and the underestimated GGA band gaps are corrected by the modified Becke-Johnson (mBJ) semilocal exchange [45]. A single-zeta polarized (SZP) atomic orbital basis set is used to capture the Kohn-Sham states without compromising accuracy, and real-space grid resolutions of approximately 0.4 Bohr for the tbBP and 0.2 Bohr for the local stacking configurations are used. Note that using 512 computing cores each with 8-GB memory, RESCU took about three wall-clock hours to converge the electronic structure calculation for the largest tbBP system (8068 atoms).

After the KS-DFT self-consistent calculations are converged, the carrier mobility μ is determined from deformation potential theory [46], which approximates full phonon scattering by long-wavelength acoustic phonon scattering, thus simplifying the analysis. The mobility values can be

TABLE I. Structural information of all tbBPs. The untwisted BP [uBP, left red BP in Fig. 1(a)] is formed by expanding the primitive cell of BP (AA stacking) with a factor of p and n along the x and y directions, respectively. The lattice mismatch is defined by the supercell length along the x and y directions ($L_{x,y}^{tBP,uBP}$) as $M_{tbBP} \equiv [(L_x^{tBP} - L_x^{uBP})/L_x^{tBP} + (L_y^{tBP} - L_y^{uBP})/L_y^{tBP}]/2$, where superscripts tBP and uBP mean twisted [Fig. 1(a) blue supercell] and untwisted BP [Fig. 1(a) red supercell], respectively.

	Twisted bilayer black phosphorus				
Twist angle	$\theta = 1.8^\circ$	$\theta = 2.2^\circ$	$\theta = 2.7^\circ$	$\theta = 3.6^\circ$	$\theta = 5.4^\circ$
Number of atoms	8068	5604	3588	2020	900
$n \times p$	24 × 42	20 × 35	16 × 28	12 × 21	8 × 14
Supercell size (Å)	140.70 × 106.35	117.25 × 88.63	93.90 × 70.98	70.35 × 53.17	47.00 × 35.35
Lattice mismatch M_{tbBP}	0.049%	0.071%	0.111%	0.198%	0.443%

considered as upper bounds. For a thin film of *finite thickness* W_{eff}, the deformation potential limited carrier mobility—derived in Ref. [47]—is

$$\mu_{\text{film}} = \frac{\pi e \hbar^4 C_{\text{film}}}{\sqrt{2}(k_B T)^{3/2}(m^*)^{5/2}(D_A)^2} F, \quad (1)$$

where F is a crossover function that bridges 2D and 3D,

$$F \equiv \frac{\sum_n \left\{\frac{\sqrt{\pi}}{2}[1 - \text{erf}(\Omega(n)] + \Omega(n) e^{-\Omega^2(n)}\right\}}{\sum_n [1 + \Omega^2(n)] e^{-\Omega^2(n)}} \quad (2)$$

and

$$\Omega(n) \equiv \sqrt{\frac{n^2 \pi^2 \hbar^2}{2 m^* {W_{\text{eff}}}^2 k_B T}}.$$

In the crossover function F, erf is the error function, the summation over integers n is due to quantum confinement along the z direction (finite thickness direction), and W_{eff} can be calculated using the wave functions obtained by KS-DFT or analytically assuming a square-well confinement potential. In Eq. (1), D_A is the deformation potential, which is defined as $\delta E_i = D_{Ai} \delta a / a$, where δE_i is the energy change of the ith electronic band under proper cell compression and dilatation, a is the lattice constant, and δa the deformation of a. C_{film} is related to the calculated elastic modulus extracted from stress-strain relation predicted by LAMMPS (details in Appendix C), with uniaxial tension in the NPT ensemble by setting the strain rate as 1×10^{-5} /fs. m^* is the calculated effective mass along the transport direction. The supercell dilation or compression (e.g., deformation) proceeds by increments of 0.5% in the subsequent KS-DFT calculations.

III. RESULTS AND DISCUSSIONS

Before calculating the supercells of tbBPs, we first analyze the four high-symmetry local stacking configurations individually. They are shown in the smaller colored rectangles in Fig. 1(b) and their geometric parameters are summarized in Table III in Appendix A. Their band structures were calculated using the GGA Perdew-Burke-Ernzerhof (PBE) functional and reported in Appendix A. We found that the band gaps of all local configurations are direct and located at the Γ point, with values 0.69 eV for AA, 0.53 eV for AB, 0.49 eV for AA', and 0.38 eV for AB'. Since GGA underestimates band gaps, we correct them by using the mBJ semilocal exchange [45] (see Appendix A), which gives band gaps 1.45 eV, 1.36 eV, 1.29 eV, and 1.21 eV for the AA, AB, AA', and AB' stackings, respectively. The mBJ exchange functional is also applied in band-gap calculation of all tbBPs.

The electronic property of the four individual local stacking configurations shall provide intuitive consideration when tbBPs are analyzed. However, the overall physical picture of the latter can only be obtained by directly calculating the tbBP supercell—the large black rectangle in Fig. 1(b)—where all the local stacking coexists to give the Moiré pattern. Structurally, we found that tbBPs are not flat-sheet but slightly corrugated into the third dimension (see Appendix B), where the out-of-plane corrugation amplitude from AB stacking to AA' stacking is ∼0.3 Å and the interlayer distance of AA (∼3.42 Å) and AB' stacking (∼3.38 Å) are similar.

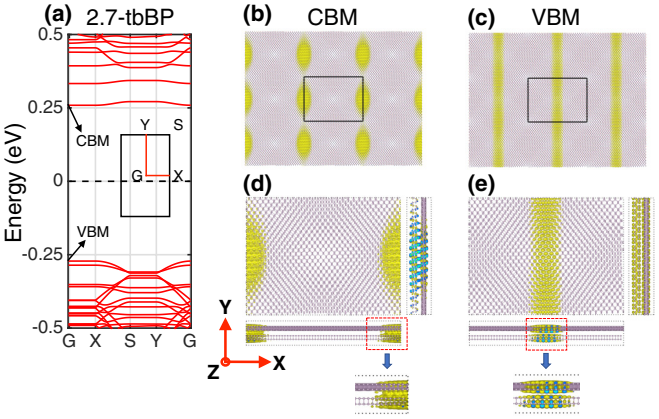

FIG. 2. (a) Calculated band structure of 2.7-tbBP. (b, c) Spatial distribution of wave functions of the periodic 2.7-tbBP Moiré structure CBM and VBM, respectively. The central black rectangle box in (b) and (c) indicates the simulated supercell of 2.7-tbBP, which contains 3588 atoms. The distribution of four stacking configurations is the same as that in Fig. 1(b). (d, e) Zoom-in on the supercells indicated by the black rectangles in (b) and (c), respectively. The isosurface value is set at 1.7×10^{-5} e Å^{-3}.

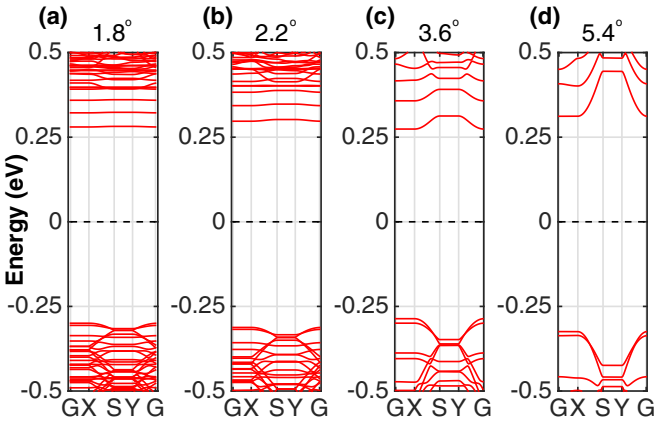

FIG. 3. The calculated band structures, at the GGA-PBE level, of four tbBPs (except 2.7-tbBP) are plotted. (a)–(d) The band structures of tbBPs with twist angle $\theta = 1.8°, 2.2°, 3.6°$, and 5.4°, respectively. The 2D Brillouin zone is the same as that in Fig. 2(a).

TABLE II. Calculated effective mass m^* in units of bare mass m_0, elastic modulus C_{film} in units of GPa, deformation potential D_A in units of eV, and mobility μ in units of 10^3 cm^2 V^{-1} s^{-1} for the tbBPs along the armchair (y) direction, corresponding to the Γ-Y direction in the 2D Brillouin zone. The subscripts e (electron) and h (hole) indicate the carrier type.

	m_e^*	m_h^*	D_{A-e}	D_{A-h}	C_{film}	μ_e	μ_h
$\theta = 0°$	0.13	0.12	4.28	3.51	44	2.56	4.46
$\theta = 1.8°$	0.84	0.16	3.44	2.99	62	0.13	4.55
$\theta = 2.16°$	0.45	0.16	3.68	3.14	63	0.41	4.48
$\theta = 2.7°$	0.29	0.16	3.58	3.18	69	1.14	4.79
$\theta = 3.6°$	0.20	0.16	3.68	3.07	68	2.25	5.06
$\theta = 5.4°$	0.17	0.16	3.38	3.17	68	3.70	4.75

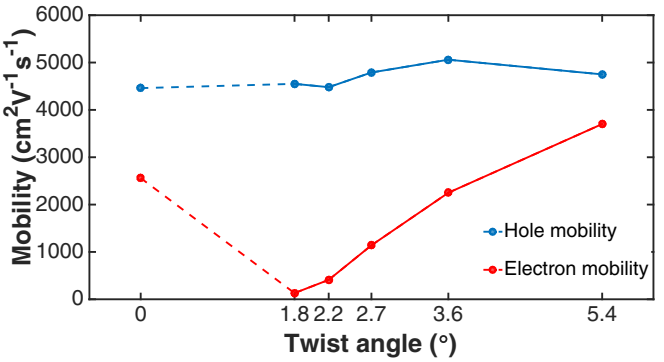

FIG. 4. Deformation limited carrier mobility along the armchair (y) direction (Γ-Y direction in k space) of tbBPs versus the twist angle θ. The dash and solid lines are guides to the eye.

The calculated band structure of the relaxed 2.7-tbBP is shown in Fig. 2(a). Compared with those of the individual local stacking configurations (see Appendix A), the most striking feature of 2.7-tbBP is the flatbands along the Γ-X and S-Y direction, with energies corresponding to CBM and VBM in the reciprocal space, corresponding to the x direction (zigzag direction) in real space. Away from CBM and VBM, dispersive bands are observed. The flatbands suggest localization of electronic states at CBM and VBM, and may lead to extraordinary carrier transport phenomena. To this end, the spatial distribution of the wave functions of CBM ($|\psi_c(\mathbf{r})|^2$) and VBM ($|\psi_v(\mathbf{r})|^2$) are plotted in Figs. 2(b) and 2(c), in which the black rectangles are the 2.7-tbBP supercells magnified in Figs. 2(d) and 2(e). Indeed, the CBM wave function ψ_c is strongly localized in all directions, while the VBM wave function ψ_v is strongly localized along the x direction but not along the y direction.

The band structures of the other four tbBPs, calculated at the GGA-PBE level, are plotted in Fig. 3 [2.7-tbBP being already plotted in Fig. 2(a)]. Similar to the 2.7-tbBP, flatbands exist. When there is no twist ($\theta = 0$), the bilayer BP has a mBJ band gap of 1.51 eV. Then the band gaps of tbBPs (Moiré structures) are found to increase, from 1.32 eV in 1.8-tbBP to 1.49 eV in 5.4-tbBP. A similar trend is also found in GGA gaps (with systematic underestimation), from 0.58 eV in 1.8-tbBP to 0.64 eV in 5.4-tbBP.

As discussed in the Introduction, if we consider the high-symmetry local stacking configurations in the Moiré pattern as large "Moiré impurities" periodically residing in an infinite tbBP, the flatbands at CBM and VBM of the tbBP can intuitively be considered as the "Moiré impurity bands." It is interesting to determine which "Moiré impurity" (local stacking configuration) is responsible for the CBM and VBM states in Figs. 2(b) and 2(c). Our results indicate that ψ_c is strongly localized on the AB' stacking and nearby transitional regions, while ψ_v is localized on the AA and AB stackings. Looking at the side view of 2.7-tbBP [right-hand side bars in Figs. 2(d) and 2(e)], ψ_c and ψ_v distribute in the two BP layers, and the localized AB' region has a strong interlayer coupling as seen in the red-dashed box in Fig. 2(d), which is consistent with the results of the high-symmetry local stacking configurations (see Appendix A).

Having understood that the carrier mobility at CBM and VBM are dominated by the flat Moiré-impurity bands characterized by the localized nature of the wave functions, we now predict the mobility of tbBP versus the twist angle θ. To this end, since the flatbands along the zigzag (x) direction lead to extremely heavy effective mass in that direction, we only need to focus on the mobility along the armchair (y) direction (Γ-Y direction in k space), calculated by Eq. (1). The calculated values of m^*, D_A, C_{film}, and mobility μ for tbBPs as well as for the bilayer BP at $\theta = 0$ (AA stacking) are presented in Table II. To make the presentation clearer, Fig. 4 plots the deformation potential limited carrier mobility along the armchair direction and several observations are in order. First, the electron mobility strikingly drops by almost 20-fold (to $\sim$131 cm^2 V^{-1} s^{-1}) when θ increases from zero to 1.8°. This dramatic effect is due to the strong localization of ψ_c along the armchair (y) direction at relatively small twist angle (see below). Second, beyond $\theta = 1.8°$, where the mobility assumes its minimum, the size of the Moiré impurities (e.g., local stacking) shrinks as θ increases and eventually blurs. The electron mobility increases as a result. Interestingly, the mobility at larger θ (i.e., 5.4°) can be larger than that at $\theta = 0$, because most material parameters appearing in Eq. (1) also vary with θ (see Table II). Third, Fig. 4 shows that the hole

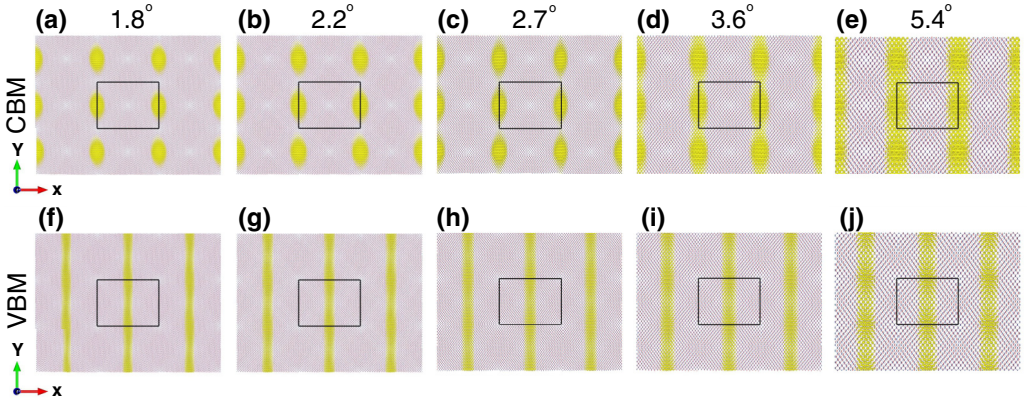

FIG. 5. (a)–(e) Spatial distribution of $|\psi_c(\mathbf{r})|^2$ of the tbBP for five twist angles. On the VBM side, the spatial distribution of $|\psi_v(\mathbf{r})|^2$ are plotted in (f)–(g). The twist angles θ are shown on the top row. The black boxes indicate the supercell of the tbBP, and the distribution of the four stacking configurations is the same as that in Fig. 1(b). The isosurface value is identical to that in Fig. 2.

mobility barely changes with respect to θ, which is demystified by plotting the real-space wave functions.

The wave-function norms $|\psi_c(\mathbf{r})|^2$ and $|\psi_v(\mathbf{r})|^2$ of the tbBPs are plotted in Fig. 5. Figures 5(a)–5(e) show that the CBM wave function ψ_c is localized along both the x and the y directions when θ is small, and at $\theta = 1.8^\circ$ the localization is the strongest, hence the electron mobility is the smallest. As θ increases, the localized ψ_c elongates along the y direction and eventually becomes delocalized. This is because the local AA' stackings become blurred as θ increases and the localized ψ_c pervades from one AA' to vicinal AA' stackings along the y direction [see Figs. 5(a)–5(e)]. This is why the electron mobility along the y direction increases with the increase of θ (after 1.8°). On the VBM side, as shown in Figs. 5(f)–5(j), ψ_v is only localized along the x direction but is extended along the y direction for all θ, because ψ_v resides on both the AA and AB stackings which are nearest neighbors to each other [see Fig. 1(b)]. This explains why the hole mobility is almost independent of θ, as presented in Fig. 4.

Note that the "Moiré impurity"-induced flatbands is somewhat reminiscent of impurity bands in crystals. When a semiconductor crystal is dilutely doped with impurity atoms, impurity bands may form inside the band gap of the semiconductor. In the dilute limit, weakly interacting impurity atoms form flat impurity bands. Rather than isolated impurity atoms, the Moiré impurity has much greater length scales, as it is formed by the high-symmetry local stacking configurations on the Moiré patterns. As a result, the wave functions localize on much larger scales than the atomic size of an impurity. Since the Moiré pattern is ubiquitous in twisted bilayers of 2D materials, the Moiré-impurity-induced localization and its significant impact on charge transport is probably not limited to tbBP but should be quite general.

IV. CONCLUSION

In conclusion, by using a state-of-the-art first-principles method that allows us to directly calculate very large tbBP structures, we discover that the Moiré patterns have extraordinary effects on electronic and transport properties, and may lead to a significant asymmetry with respect to transport direction and carrier type. In particular, the high-symmetry local stacking configurations in Moiré superlattices act as impurities with sizes on the order of the Moiré length scale, and hence are called "Moiré impurities." These Moiré impurities induce flatbands and localized states in tbBPs. Because both CBM and VBM are dominated by these localized states, the deformation potential limited carrier mobility is significantly affected. Along the zigzag or x direction, CBM and VBM states are strongly localized and both the electron and hole mobilities are small. Along the armchair or the y direction, the CBM state is localized at small twist angles and the electron mobility at $\theta = 1.8^\circ$ ($\sim$131 $\mathrm{cm^2\,V^{-1}\,s^{-1}}$) is almost 20 times smaller than that at zero angle ($\sim$2560 $\mathrm{cm^2\,V^{-1}\,s^{-1}}$). When the twist angle θ increases, the high-symmetry local stacking responsible for the localized CBM state becomes blurred and the localized states on nearby local stacking configurations overlap, weakening the localization; hence the electron mobility increases. On the VBM side, the hole mobility along the armchair or y direction is almost independent of θ, which is again due to the wave function pervading through the AA and AB local stacking configurations.

Given the tremendous progress in fabricating and characterizing 2D vdW heterojunction materials, our prediction of the Moiré-impurities-induced wave-function localization and the concomitant drastic reduction of the carrier mobility should be experimentally verifiable, and it could provide an interesting strategy for designing nanoelectronic devices. Besides, on the

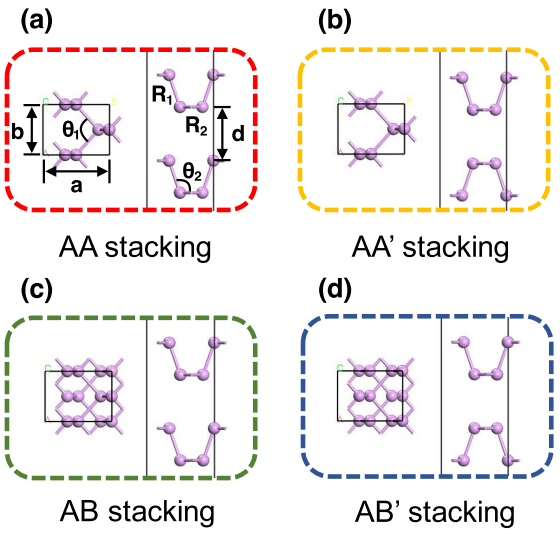

FIG. 6. High-symmetry local stacking configurations. The detailed geometrical parameters are summarized in Table III.

TABLE III. Optimized geometric parameters of the four high-symmetry stacking configurations. a and b are lattice constants. d denotes the interlayer distance. R_1 and R_2 are the bond lengths and θ_1 and θ_2 indicate the bond angles. The unit of length is Å.

Type	$a \times b$	d	R_1	R_2	θ_1	θ_2
AA	4.541 × 3.315	3.487	2.363	2.259	94.387°	102.297°
AB	4.433 × 3.321	3.219	2.158	2.237	95.863°	102.956°
AA'	4.548 × 3.323	3.681	2.147	2.264	94.436°	103.557°
AB'	4.538 × 3.331	3.453	2.411	2.258	95.030°	101.925°

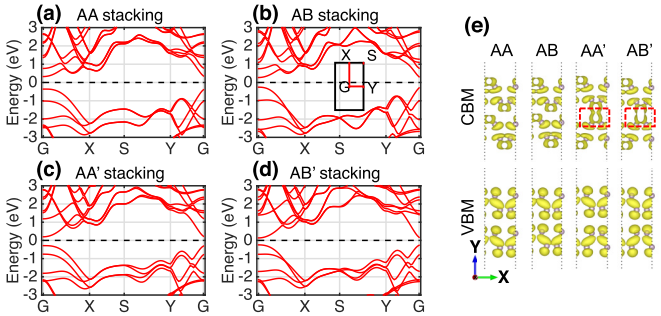

FIG. 7. The electronic properties of four high-symmetry local stacking configurations. The calculated band structures of (a) AA stacking, (b) AB stacking, (c) AA' stacking, and (d) AB' stacking are plotted. (e) The spatial distribution of partial charge density (wave functions) corresponding to VBM and CBM using an isosurface of 1.5 $\times 10^{-3}\ e$ Å^{-3}.

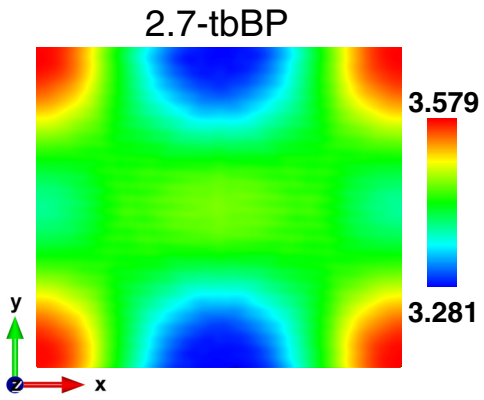

FIG. 8. Contour plot of the interlayer distance between two constituent layers of 2.7-tbBP supercell in Å. The distribution of four stacking configurations in tbBP is the same as those in Fig. 1(b) of the main text.

physics side, electron scattering at the well-defined Moiré-impurity boundaries may cause Friedel oscillation [48] of the charge density, especially for situations when the boundaries of high-symmetry scattering local configurations are very well defined. We hope to report this and other interesting physical phenomenon associated with the Moiré impurities in the future.

ACKNOWLEDGMENTS

We wish to thank Y.-C. Chen and Q. Shi for useful discussions on the exchange-correlation functional used in this work. This work is financially supported by the NSERC of Canada and FQRNT of Quebec (H.G.). P.K. thanks the China Scholarship Council (No. 201506460039) for a CSC fellowship and is thankful for the hospitality of McGill University, where this work was done. We thank Compute Canada and the High Performance Computing Center of McGill University for the computer facilities and support which made this work possible.

APPENDIX A: ELECTRONIC BANDS OF LOCAL STACKING CONFIGURATIONS

In this Appendix, we present (i) the calculated electronic structures of the four high-symmetry local stacking configurations, and (ii) some details regarding the mBJ semilocal exchange [45], which we implemented into the real-space KS-DFT code RESCU [41] and used to calculate band gaps.

The four high-symmetry local stacking configurations are plotted in Fig. 6, corresponding to Fig. 1(b) in the main text, and the detailed geometric parameters of them are listed in Table III. The AA stacking, in which the upper layer is exactly stacked on the top of the lower layer, has *Pmma* symmetry; the AB stacking, in which the upper layer of AA stacking is shifted by half of a unit cell, has *Pbcm* symmetry; the AA' stacking, in which the upper layer of AA stacking is shifted by one unit cell and the two constituent layers are mirror images of each other from the side view, has *Pmma* symmetry; the AB' stacking, in which the upper layer of AA' stacking is shifted by half of a unit cell, has *Pccm* symmetry.

The band gaps of the local stacking configurations and tbBPs are corrected by the mBJ semilocal exchange potential [45],

$$v_x^{\mathrm{mBJ}}(\boldsymbol{r}) = c\,v_x^{\mathrm{BR}}(\boldsymbol{r}) + (3c-2)\frac{1}{\pi}\sqrt{\frac{5}{12}}\sqrt{\frac{2t(\boldsymbol{r})}{\rho(\boldsymbol{r})}}, \tag{A1}$$

where c is given by

$$c = A + B\sqrt{g} \tag{A2}$$

and

$$g = \frac{1}{V_{\mathrm{cell}}}\int_{\mathrm{cell}}\frac{|\nabla\rho(\boldsymbol{r})|}{\rho(\boldsymbol{r})}d^3r. \tag{A3}$$

Following Ref. [45], $v_x^{\mathrm{BR}}(\boldsymbol{r})$ is the Becke-Roussel (BR) potential which models the Coulomb potential of the exchange hole. A and B are two parameters, $A = -0.012$ and $B = 1.023$ Bohr$^{1/2}$, according to a fit to the experimental band gaps [49]. Here the material-dependent parameter c is extracted based on band structure data obtained from hybrid functional HSE06 calculations executed by RESCU. By setting $c = 1.348$, the band gaps obtained by semilocal exchange mBJ (1.78 eV for mono-BP) are consistent with those predicted by HSE06. The same c value is applied when calculating band gaps of tbBPs.

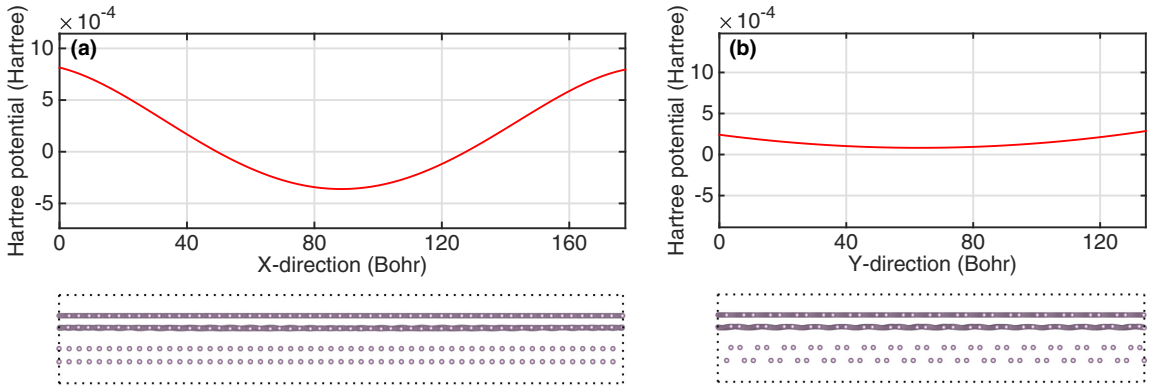

FIG. 9. Calculated averaged Hartree potential of 2.7-tbBP supercell projected along (a) the zigzag or x direction and (b) armchair or y direction. The corresponding schematics of side views are plotted below the Hartree potential.

The calculated band structures, at the GGA-PBE level, of the four stacking configurations are plotted in Figs. 7(a)–7(d). The AB stacking bilayer is the most energetically favorable configuration. In addition, we calculate the spatial distribution of partial charge densities corresponding to VBM and CBM of the four stacking configurations [Fig. 7(e)]. A stronger interlayer interaction causes the wave-function overlap [red dash box in Fig. 7(e)] in the AA' and AB' stacking patterns. Note that the electronic bands of the AA stacking, which correspond to the untwisted bilayer [Fig. 7(a)], have significant dispersions, which is distinctively different from those of the Moiré patterns at nonzero twist angles.

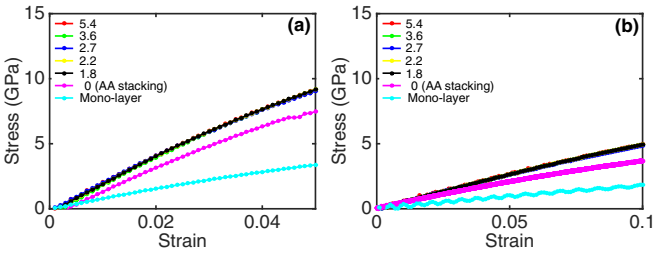

FIG. 10. Linear regime of the stress-strain relation under uniaxial tension: (a) along zigzag or x direction and (b) armchair or y direction, as obtained by LAMMPS simulations.

APPENDIX B: CORRUGATION AND POTENTIAL OF 2.7-TBBP

In this Appendix, we present the relaxed structure of the 2.7-tbBP, which corrugates into the z direction. The out-of-plane corrugation amplitude of 2.7-tbBP is plotted in Fig. 8. During the structural relaxation, we keep the uBP layer fixed and optimize the atomic structure of the tBP layer, and thereby the interlayer distance d [see Fig. 6(a)] is determined.

The calculated averaged Hartree potential of the 2.7-tbBP projected along the x and y direction are extracted as shown in Fig. 9. Both the interlayer distance and the averaged Hartree potential profile indicate that the relaxed 2.7-tbBP (and other tbBPs) is corrugated into the third dimension.

APPENDIX C: LINEAR STRESS-STRAIN RELATION OF TBBPS

In this Appendix, we present the calculated stress-strain relation of tbBP, which gives the elastic modulus C_{film} in Eq. (1). The molecular dynamics (MD) simulation of the linear stress-strain relations under uniaxial tension along x and y directions are presented in Figs. 10(a) and 10(b), as well as for AA stacking and monolayer black phosphorus. The C_{film} is calculated based on the definition $C_{\text{film}} = \partial\sigma_s/\partial\varepsilon$, where σ_s indicates the stress under the linear stress-strain relations and the ε is the corresponding strain. Compared to the untwisted bilayer BP (the pink dotted line in Fig. 10), the enhancement of elastic constant for tbBPs along both directions is clearly observed from the stress-strain relations.

[1] A. K. Geim and K. S. Novoselov, Nat. Mater. **6**, 183 (2007).
[2] M. Xu, T. Liang, M. Shi, and H. Chen, Chem. Rev. **113**, 3766 (2013).
[3] S. Z. Butler, S. M. Hollen, L. Cao, Y. Cui, J. A. Gupta, H. R. Gutiérrez, T. F. Heinz, S. S. Hong, J. Huang, A. F. Ismach, E. Johnston-Halperin, M. Kuno, V. V. Plashnitsa, R. D. Robinson, R. S. Ruoff, S. Salahuddin, J. Shan, L. Shi, M. G. Spencer, M. Terrones, W. Windl, and J. E. Goldberger, ACS Nano **7**, 2898 (2013).
[4] G. Fiori, F. Bonaccorso, G. Iannaccone, T. Palacios, D. Neumaier, A. Seabaugh, S. K. Banerjee, and L. Colombo, Nat. Nanotechnol. **9**, 768 (2014).
[5] A. K. Geim and I. Grigorieva, Nature (London) **499**, 419 (2013).
[6] K. Novoselov, A. Mishchenko, A. Carvalho, and A. C. Neto, Science **353**, aac9439 (2016).
[7] Y. Liu, N. O. Weiss, X. Duan, H.-C. Cheng, Y. Huang, and X. Duan, Nat. Rev. Mater. **1**, 16042 (2016).
[8] M.-Y. Li, C.-H. Chen, Y. Shi, and L.-J. Li, Mater. Today **19**, 322 (2016).
[9] W. Zhang, Q. Wang, Y. Chen, Z. Wang, and A. T. Wee, 2D Mater. **3**, 022001 (2016).
[10] Y. Zhang, A. Rubio, and G. Le Lay, J. Phys. D Appl. Phys. **50**, 053004 (2017).
[11] G. Giovannetti, P. A. Khomyakov, G. Brocks, P. J. Kelly, and J. van den Brink, Phys. Rev. B **76**, 073103 (2007).
[12] C. R. Dean, A. F. Young, I. Meric, C. Lee, L. Wang, S. Sorgenfrei, K. Watanabe, T. Taniguchi, P. Kim, K. L. Shepard, and J. Hone, Nat. Nanotechnol. **5**, 722 (2010).
[13] R. Decker, Y. Wang, V. W. Brar, W. Regan, H.-Z. Tsai, Q. Wu, W. Gannett, A. Zettl, and M. F. Crommie, Nano. Lett. **11**, 2291 (2011).
[14] J. Kang, J. Li, S.-S. Li, J.-B. Xia, and L.-W. Wang, Nano. Lett. **13**, 5485 (2013).
[15] C.-H. Lee, G.-H. Lee, A. M. Van Der Zande, W. Chen, Y. Li, M. Han, X. Cui, G. Arefe, C. Nuckolls, T. F. Heinz, J. Guo, J. Hone, and P. Kim, Nat. Nanotechnol. **9**, 676 (2014).
[16] H. Fang, C. Battaglia, C. Carraro, S. Nemsak, B. Ozdol, J. S. Kang, H. A. Bechtel, S. B. Desai, F. Kronast, A. A. Unal, G. Conti, C. Conlon, G. K. Palsson, M. C. Martin, A. M. Minor, C. S. Fadley, E. Yablonovitch, R. Maboudian, and A. Javey, PNAS **111**, 6198 (2014).
[17] G. Trambly de Laissardiere, D. Mayou, and L. Magaud, Nano Lett. **10**, 804 (2010).
[18] T. Ohta, J. T. Robinson, P. J. Feibelman, A. Bostwick, E. Rotenberg, and T. E. Beechem, Phys. Rev. Lett. **109**, 186807 (2012).
[19] G. Li, A. Luican, J. L. Dos Santos, A. C. Neto, A. Reina, J. Kong, and E. Andrei, Nat. Phys. **6**, 109 (2010).
[20] S. Dai, Y. Xiang, and D. J. Srolovitz, Nano. Lett. **16**, 5923 (2016).
[21] Y. Cao, J. Y. Luo, V. Fatemi, S. Fang, J. D. Sanchez-Yamagishi, K. Watanabe, T. Taniguchi, E. Kaxiras, and P. Jarillo-Herrero, Phys. Rev. Lett. **117**, 116804 (2016).
[22] B. Hunt, J. Sanchez-Yamagishi, A. Young, M. Yankowitz, B. J. LeRoy, K. Watanabe, T. Taniguchi, P. Moon, M. Koshino, P. Jarillo-Herrero, and R. C. Ashoori, Science **340**, 1427 (2013).

[23] Q. Tong, H. Yu, Q. Zhu, Y. Wang, X. Xu, and W. Yao, Nat. Phys. **13**, 356 (2017).
[24] L. Li, Y. Yu, G. J. Ye, Q. Ge, X. Ou, H. Wu, D. Feng, X. H. Chen, and Y. Zhang, Nat. Nanotechnol. **9**, 372 (2014).
[25] A. S. Rodin, A. Carvalho, and A. H. Castro Neto, Phys. Rev. Lett. **112**, 176801 (2014).
[26] J. Qiao, X.-H. Kong, Z.-X. Hu, F. Yang, and W. Ji, Nat. Commun. **5**, 4475 (2014).
[27] X. Zhou, R. Zhang, J. Sun, Y. Zou, D. Zhang, W. Lou, F. Cheng, G. Zhou, F. Zhai, and K. Chang, Sci. Rep. **5**, 12295 (2015).
[28] X. Zhou, W.-K. Lou, D. Zhang, F. Cheng, G. Zhou, and K. Chang, Phys. Rev. B **95**, 045408 (2017).
[29] F. Xia, H. Wang, and Y. Jia, Nat. Commun. **5**, 4458 (2014).
[30] R. Zhang, X. Zhou, D. Zhang, W. Lou, F. Zhai, and K. Chang, 2D Mater. **2**, 045012 (2015).
[31] X. Zhou, W.-K. Lou, F. Zhai, and K. Chang, Phys. Rev. B **92**, 165405 (2015).
[32] L. Li, F. Yang, G. J. Ye, Z. Zhang, Z. Zhu, W. Lou, X. Zhou, L. Li, K. Watanabe, T. Taniguchi, K. Chang, Y. Wang, X. H. Chen, and Y. Zhang, Nat. Nanotechnol. **11**, 593 (2016).
[33] M. Wu, X. Qian, and J. Li, Nano. Lett. **14**, 5350 (2014).
[34] J. Dai and X. C. Zeng, J. Phys. Chem. Lett. **5**, 1289 (2014).
[35] H. Shu, Y. Li, X. Niu, and J. Wang, Phys. Chem. Chem. Phys. **18**, 6085 (2016).
[36] K. Uchida, S. Furuya, J.-I. Iwata, and A. Oshiyama, Phys. Rev. B **90**, 155451 (2014).
[37] S. Plimpton, J. Comput. Phys. **117**, 1 (1995).
[38] J.-W. Jiang, Nanotechnology **26**, 315706 (2015).
[39] J.-W. Jiang and H. S. Park, J. Appl. Phys. **117**, 124304 (2015).
[40] C. Hu, V. Michaud-Rioux, X.-H. Kong, and H. Guo (unpublished).
[41] V. Michaud-Rioux, L. Zhang, and H. Guo, J. Comput. Phys. **307**, 593 (2016).
[42] Y. Zhou, Y. Saad, M. L. Tiago, and J. R. Chelikowsky, Phys. Rev. E **74**, 066704 (2006).
[43] D. R. Hamann, Phys. Rev. B **88**, 085117 (2013).
[44] J. P. Perdew, K. Burke, and M. Ernzerhof, Phys. Rev. Lett. **77**, 3865 (1996).
[45] F. Tran and P. Blaha, Phys. Rev. Lett. **102**, 226401 (2009).
[46] J. Bardeen and W. Shockley, Phys. Rev. **80**, 72 (1950).
[47] P. Kang, V. Michaud-Rioux, X.-H. Kong, G.-H. Yu, and H. Guo, 2D Mater. **4**, 045014 (2017).
[48] Y.-L. Zou, J. Song, C. Bai, and K. Chang, Phys. Rev. B **94**, 035431 (2016).
[49] D. Koller, F. Tran, and P. Blaha, Phys. Rev. B **85**, 155109 (2012).